The Nanopyramidal Reconstruction of Cu 2 O(111): a Long-standing Surface Puzzle Solved by STM and DFT

A. Gloystein, N. Nilius, J. Goniakowski, C. Noguera

The Nanopyramidal Reconstruction of $Cu_2O(111)$: a Long-standing Surface Puzzle Solved by STM and DFT.

A. Gloystein,[†] N. Nilius,[*,†] J. Goniakowski,[*,‡] and C. Noguera[‡]

[†]*Institut für Physik, Carl von Ossietzky Universität, D-26111 Oldenburg, Germany*
[‡]*CNRS-Sorbonne Université, UMR 7588, INSP, F-75005 Paris, France*

E-mail: niklas.nilius@uni-oldenburg.de; jacek.goniakowski@insp.jussieu.fr

Abstract

Despite the importance of cuprous oxide for industrial applications, the precise structure of its most stable reconstructed surface remains unknown. Here, by a combination of high-resolution STM measurements and simulations based on a DFT-HSE approach, we challenge the previous interpretations of the $Cu_2O(111)$ $(\sqrt{3}\times\sqrt{3})$R30° surface reconstruction, based on the removal of 1/3 of the under-coordinated surface oxygen atoms. We show that these models do not satisfy the shamrock-type features found by STM, i.e. their position in the Cu-O ring centers, the orientation towards the surface O_{cus} atoms and the topographic height in the STM images. Moreover, they are thermodynamically unstable with respect to moving the vacancy subsurface, a property not recognized before which seems specific to the Cu_2O (111) surface. We propose a nanopyramidal model of the $(\sqrt{3}\times\sqrt{3})$R30° surface reconstruction which is free from all these shortcomings. Here, the shamrock protrusions seen in STM are formed by three copper adatoms located at the center of the Cu-O rings and capped by an oxygen atom. This structure profoundly differs from existing models of the $Cu_2O(111)$ surface, and would change common perceptions on its reactivity.

1 Introduction

Cuprous oxide Cu_2O is a widespread oxide formed in the first stages of corrosion of copper. It is a p-type semiconductor, with applications in photovoltaics and photocatalysis. As a catalyst it is widely used in water-gas shift reactions, methanol synthesis and partial oxidation. Precise knowledge of its surfaces properties is thus of paramount importance to foster its applications. This is why Cu_2O surfaces have been extensively studied.[1–15]

Cu_2O surface structures, mainly along the (100) and (111) orientations have been studied by a variety of surface science methods.[1] Several LEED patterns have been recorded at the (100) surface, featuring (1×1), $c(2 \times 2)$ and (3,0;1,1) periodicities, and some model structures based on STM measurements and DFT simulations have been proposed.[2–5]

Cuprous oxide Cu_2O crystallizes in a cubic structure in which Cu and O atoms are coordinatively saturated with two and four first neighbors, respectively (hereafter referred to as Cu_{csa} and O_{csa}). The oxygen ions form a bcc lattice and are surrounded by a tetrahedron of copper ions. Along the (111) orientation, the structure may be seen as a stacking of neutral and dipole-free O-4Cu-O trilayer repeat units. The stoichiometric O-terminated surface (referred to as ST in Figure 1) exposes an equal number of under-coordinated oxygen O_{cus} and copper Cu_{cus} ions, characterized by the loss of one first

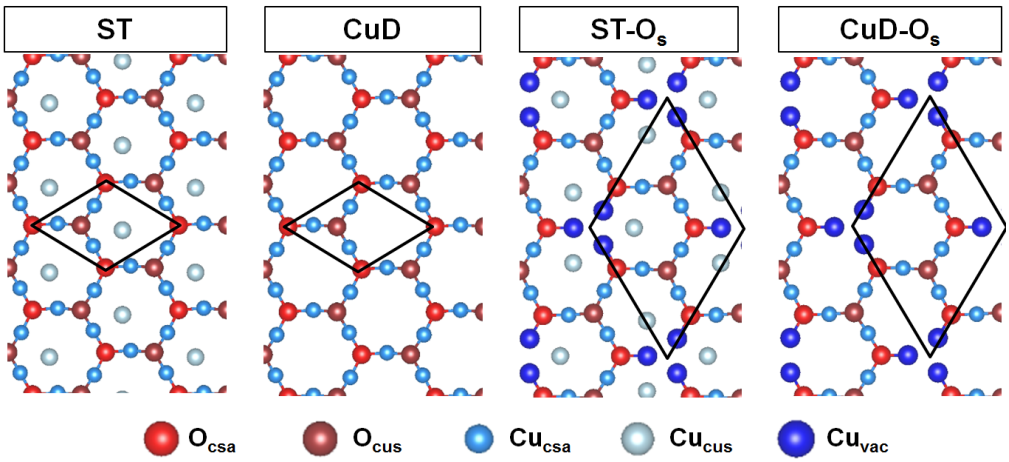

Figure 1: Atomic structure of the stoichiometric (ST) and Cu-deficient (CuD) (1×1) $Cu_2O(111)$ surface and the two vacancy models of $(\sqrt{3} \times \sqrt{3})R30°$ reconstruction, built by removing 1/3 O_{cus} atoms from either the stoichiometric (ST-O_s) or Cu-deficient (CuD-O_s) surfaces. (1×1) and $(\sqrt{3} \times \sqrt{3})R30°$ unit cells and color codes for atoms are indicated. The three copper atoms Cu_{vac} in the direct vicinity of the oxygen vacancies are represented with a dark blue color.

neighbor compared to the bulk crystal. The O_{cus} ions are positioned in the corners of the Cu_6O_6 rings, and the Cu_{cus} ions, bonded to a sub-surface oxygen ion, are located in the ring centers. A Cu_{cus}-deficient termination (CuD in Figure 1) obtained by removing all copper Cu_{cus} ions, also displays a (1×1) periodicity.

Both (1×1) and $(\sqrt{3} \times \sqrt{3})R30°$ surface periodicities have been experimentally recorded along this orientation, which were initially attributed to the stoichiometric and an oxygen-deficient configuration, respectively.[1] Later on, the (1 x 1)-$Cu_2O(111)$ surface has been explored by STM on bulk samples[6] and ultra-thin metal-supported films.[7–9] Its hexagonal pattern exhibits symmetry and spacing consistent with both Cu_{cus} and O_{cus} atoms, which does not allow to discriminate between the stoichiometric and the Cu-deficient termination.[10–13]

The reconstructed $(\sqrt{3} \times \sqrt{3})R30°$ surface, which is the subject of the present work, arouse much interest in the community. Relying on LEED[1] and STM,[6,14] it has been interpreted as a configuration in which one third of the surface O_{cus} atoms are missing, whether in the absence or presence of the unsaturated Cu_{cus} atoms (configurations CuD-O_s or ST-O_s in Fig. 1, respectively). The former was predicted to be the most stable in the whole range of attainable oxygen chemical potentials in DFT+U approach.[15]

However, despite the importance of this issue, the actual atomic structure of this surface reconstruction remains ambiguous, since many other surface configurations combining added or removed copper or oxygen atoms on the surface or sub-surface could be compatible with the $(\sqrt{3} \times \sqrt{3})R30°$ periodicity. Moreover, GGA approaches (whether pure GGA or GGA+U) without explicit inclusion of exchange terms have already been proved to provide wrong predictions on polar surface stability in Cu_2O,[13] so that simulations based on more advanced exchange-correlation functionals are needed to determine the configurations of lowest energy.

For these reasons, the present work is devised as a combination of high-resolution STM measurements on the $Cu_2O(111)$ $(\sqrt{3}\times\sqrt{3})R30°$ reconstructed surface, and simulations based on a DFT-HSE approach. The experimental results irrevocably invalidate the vacancy models by disclosing the location and orientation of the adatoms responsible for shamrock-shaped STM contrast. Among an extensive set of surface configurations, numerical simulations reveal a new configuration consistent with all the topographic characteristics derived from our high resolution STM images and being thermodynamically the most stable in the whole range of oxygen chemical potentials. This nanopy-

ramidal model for the $(\sqrt{3} \times \sqrt{3})$R30° surface reconstruction involves Cu_4O entities formed by three copper adatoms located at the center of the Cu-O rings on-top a Cu_{cus} atom and capped by an oxygen atom. The structural and electronic characteristics of the nanopyramids – atom coordination, absence of dangling bonds, charge state – strongly differ from those present in the vacancy models, and should have an incontestable impact on the surface reactivity.

2 Methods

2.1 Experimental Methods

The experiments have been carried out in an ultrahigh-vacuum chamber ($p \approx 2{*}10^{-10}$ mbar) equipped with a liquid-nitrogen cooled scanning tunneling microscope (STM) and common surface-science tools for sample preparation and analysis. The Cu_2O films were prepared by depositing ≈10 ML of high-purity copper on an Au(111) single crystal, followed by a high-pressure oxidation in 50 mbar oxygen and 450 K. An oxidation pressure in the mbar regime turned out to be crucial to prepare oxide films thick enough to develop bulk-like properties. Low-pressure films, on the other hand, exhibit terminations that are unknown for bulk crystals, as discussed in Refs.[7,8,13] To promote long-range ordering, the samples have been post-annealed in front of an oxygen nozzle ($p \approx 10^{-4}$ mbar) at about 650 K for 20 min. The stoichiometry of so prepared oxide layers was determined with X-ray photoelectron spectroscopy to be compatible with cuprous oxide (Cu_2O). Also, the sharp, hexagonal spot pattern seen in low-energy electron diffraction (LEED) was found to match the (1×1) lattice of $Cu_2O(111)$. In addition, a $(\sqrt{3} \times \sqrt{3})$R30° superstructure became discernable in LEED, pointing to a surface reconstruction (Fig.2, inset). A similar reconstruction was earlier found on the (111) surface of bulk Cu_2O crystals.[1,14]

2.2 Computational Methods

Calculations have been performed within the DFT framework implemented in VASP.[16,17] Beyond standard GGA (PW91),[18] the hybrid (HSE06)[19,20] approximation to the exchange-correlation functional has been used as to improve the description of the Cu_2O band gap. The calculated HSE gap width (1.96 eV) increases significantly over the GGA one (0.4 eV) and is close to the experimental value of 2.15 eV.[21] Let us note that the HSE gap is also much larger than those obtained within GGA+U approximation (0.5-0.8 eV, for U = 2-8 eV, respectively).[15] While HSE significantly improves the calculated electronic structure, it impacts only little the bulk and surface structural characteristics. We find bulk Cu_2O lattice parameters of 4.31 Å and 4.29 Å in HSE and GGA, respectively, compared to the experimental value of 4.27 Å. Finally, it is worth reminding that an isolated O_2 molecule does not suffer in HSE from the overbinding typical for GGA functionals (calculated O_2 dissociation energy is equal to 4.9 and 6.4 eV in HSE and GGA, respectively).

The interaction of valence electrons with ionic cores is described within the projector augmented wave method.[22] Standard copper, and soft oxygen (energy cutoff of 270 eV) pseudopotentials provided by VASP were used in all bulk and surface calculations, enabling a complete structural relaxation at the hybrid level for all considered systems. GGA results obtained with the soft and the full (energy cutoff of 400 eV) oxygen pseudopotential were confronted and showed very satisfactory agreement (difference of bulk Cu_2O lattice parameter smaller than 0.01 Å, difference of (1×1) surface energies below 0.002 eV/Å^2).

The $Cu_2O(111)$ surfaces are modelled with symmetric slabs composed of four O-4Cu-O trilayers, at the calculated in-plane lattice parameter of bulk Cu_2O (6.10/6.07 Å in GGA/ HSE, respectively). We use asymmetric slabs with one bare (labeled B in the following) and one fully hydroxylated termination (labeled H) to improve the convergence with respect to the slab thickness. The latter is the stoichiometric $Cu_2O(111)$ termination with 3 dissociated water molecules per $(\sqrt{3} \times \sqrt{3})$R30° surface unit cell. Total surface energies of asymmetric slabs as a function of oxygen chemical potential $\Delta\mu_O$

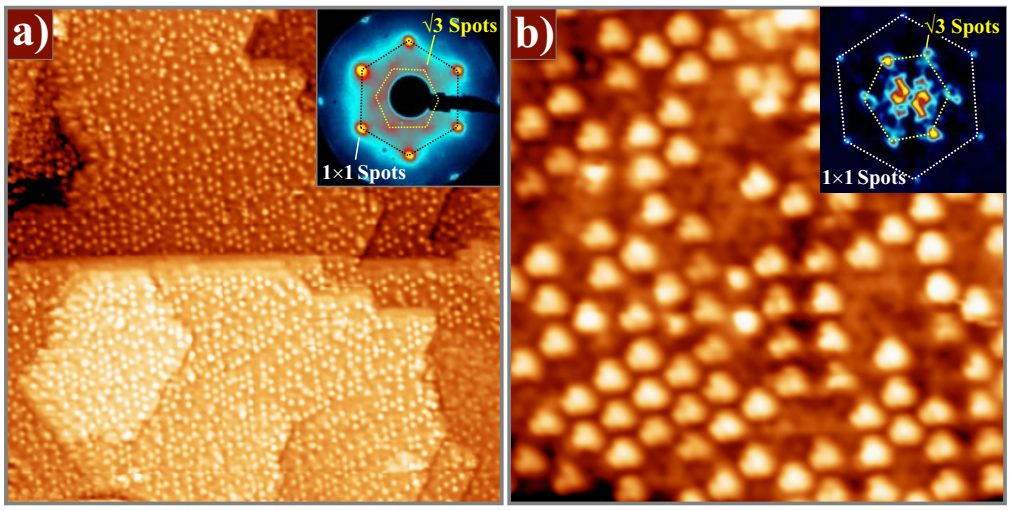

Figure 2: (a) Overview (60×60 nm^2) and (b) close-up (10.5×10.5 nm^2) STM topographic image of a high-pressure Cu_2O film on Au(111) (U_B = -1.1 V, I = 50 pA). The insets in (a) and (b) show a LEED pattern (E_{kin} = 37.5 eV) and a Fast-Fourier transformation of the oxide surface, respectively, and depict the fundamental (1×1) lattice and $(\sqrt{3} \times \sqrt{3})$R30° superstructure spots due to the protruding shamrock units.

are estimated with usual ab-initio thermodynamics expression:[23]

$$\sigma_{\mathrm{B}}(\mu_{\mathrm{O}}) + \sigma_H(\mu_{\mathrm{O}}) = \frac{(E^{a-slab}_{\mathrm{Cu_2O}} - E^{bulk}_{\mathrm{Cu_2O}} - 3E_{\mathrm{H_2O}} - \Delta N_{\mathrm{O}}(\frac{1}{2}E^{gas}_{\mathrm{O_2}} + \Delta\mu_{\mathrm{O}}))}{S}$$

where $E^{a-slab}_{\mathrm{Cu_2O}}$ is the energy of the asymmetric slab, ΔN_{O} is the number of excess oxygen atoms with respect to the Cu_2O stoichiometry, and $E_{\mathrm{H_2O}}$ is the total energy of a water molecule. S is the surface area of the $(\sqrt{3} \times \sqrt{3})$R30° unit cell. Since the evaluation of σ_{B} requires the knowledge of σ_{H}, the total energy of a symmetric slab with both terminations equivalently hydroxylated with 3 water molecules each was also calculated.

In all calculations, slabs are separated by at least 10 Å of vacuum and dipole correction is applied to slabs with two non-equivalent terminations. For the most relevant configurations, we have additionally checked that increasing the vacuum thickness up to 15 Å changes the total slab energy by less than 0.01 eV. Such supercells with more vacuum were actually used in simulations of STM images. The Brillouin zone of the $(\sqrt{3} \times \sqrt{3})$R30° surface unit cell is sampled with a $(2 \times 2 \times 1)$ Monkhorst-Pack k-point grid.[24] Atomic coordinates of all ions in the oxide film are relaxed until residual forces dropped below 0.01 eV/Å.

Simulations of STM images rely on the Tersoff-Hamann approximation. We have determined the computational settings which provide the best matching of the simulated and experimental STM images of the Cu-deficient termination. As shown in the SI Figure S1, the conventional value of 2.5*10^{-8} e/Å^3 for the isodensity surface provides the most satisfactory matching for both positive and negative biases and is systematically used.

3 Experimental Results

STM topographic images of the $Cu_2O(111)$ surface reveal wide, flat terraces that are entirely covered by nanometer-sized protrusions of ≈1.5 Å height (Fig. 2a, b). The protrusions, being referred to as shamrocks in the following, are arranged on an incomplete hexagonal lattice with 10.5 Å periodicity. This distribution is readily assigned to the $(\sqrt{3} \times \sqrt{3})$R30° superstructure seen in LEED (Fig. 2 inset), although only 40-50% of the lattice sites are actually filled with the shamrock units. In larger openings of the $(\sqrt{3} \times \sqrt{3})$R30° reconstruction, the fundamental (1×1) lattice of $Cu_2O(111)$ is

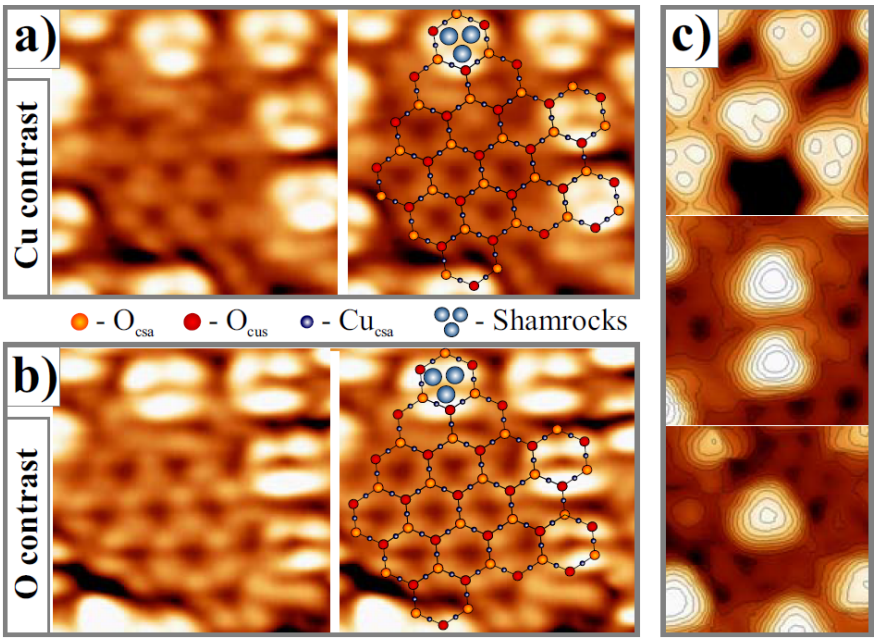

Figure 3: STM topography of a pristine Cu_2O (1×1) region with a few shamrock protrusions at the edges $(3 \times 3\ nm^2)$. While individual Cu ions are resolved in (a) (U_B = -1.1 V), the O ions are detected in (b) (U_B = +2.0 V). With this insight, a structure model may be derived for Cu_2O (1×1), in which the shamrock units occupy the centers of Cu-O six rings. (c) STM appearance of the shamrock species for characteristic tip states ($3 \times 3\ nm^2$, U_B = +2.0 V, I = 50 pA).

resolved. Two distinct contrast schemes are distinguished, both showing the porous nature of the bulk-cut $Cu_2O(111)$ surface, as composed of Cu-O six rings (Fig. 3a,b). In the first scheme, each surface pore is delimited by three atom-sized triangles comprising the Cu ions in the Cu_6O_6 rings. The respective imaging scheme has thus been labelled "copper contrast" and occurs mostly at negative sample bias. The oxygen contrast, on the other hand, reveals six protrusions on the Cu_6O_6 rings that are readily assigned to the surface O ions. Hereby, chemically saturated (O_{csa}) and unsaturated (O_{cus}) O ions alternate along the ring, with the O_{cus} species appearing slightly brighter in the STM. In both contrast schemes, the center of Cu-O six rings remains dark, suggesting that the Cu_{cus} ions that would be expected at those positions are not available in the surface. This conclusion is consistent with the characteristics of simulated STM images of the stoichiometric and Cu-deficient (1×1) surfaces (see Supporting Information (SI), Figure S1).

By correlating the atomically-resolved STM images of (1×1) patches with a model of bulk-cut $Cu_2O(111)$, the topographic position of the shamrock units can be determined. The shamrocks exclusively locate in the Cu-O ring centers, while corner or edge positions are not populated. The neighboring rings to a shamrock site always remain empty, which gives rise to the characteristic $(\sqrt{3} \times \sqrt{3})R30°$ superstructure seen in reciprocal space. Typical shamrock features protrude the Cu_2O surface by about 1.5 Å with slightly smaller values at positive compared to negative bias. A bias-independent shamrock height points to a topographic instead of an electronic contrast regime. The mean height of 1.5 Å hereby matches an extra layer of atoms sitting on top of the ideal (1×1) plane. The shamrocks typically exhibit a trifold symmetry that can sometimes be resolved into three discernable maxima (Fig. 3c). The mean distance between the shamrock's symmetry centers has been determined to 3.5 Å, although their exact STM appearance is governed by the tip shape (Fig. 3c). The shamrock units arrange into small domains containing not more than 100 individual species. Neighboring domains are separated by boundaries, along which

more than one Cu-O six ring remains unoccupied.

The only other surface irregularities besides the shamrocks are surface O vacancies, whereby only the O_{cus} ions are affected. The density of this defect type is very low, typically smaller than 0.04 nm^{-2}. In contrast to the shamrock features, the O_{cus} defects exhibit a pronounced bias-dependent contrast (Fig. 4a). They appear bright in topographic images taken above 2.0 V, but develop a negative contrast at low positive and negative bias. Whereas the O_{cus} vacancies are difficult to be identified in topographic data, they leave a clear fingerprint in the STM conductance maps (Fig. 4b). Especially at 2.3 V, they stick out due to their large conductance values, but merge with the background signal of the oxide film at lower bias. The fact that surface O vacancies are resolvable in the STM, but are clearly unrelated to the $(\sqrt{3} \times \sqrt{3})R30°$ reconstruction, invalidates the existing models of the $Cu_2O(111)$ surface in the literature.

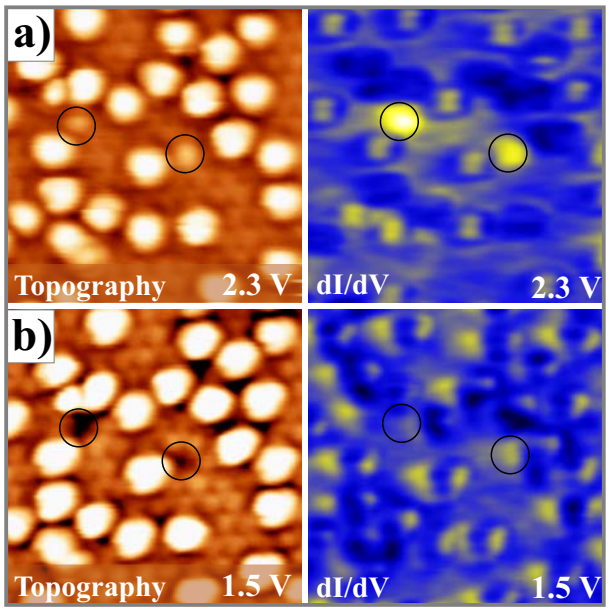

Figure 4: STM images (left) and corresponding differential conductance maps (right) of a $Cu_2O(111)$ surface with shamrock maxima, measured with oxygen contrast (6×6 nm^2, I = 50 pA). The two encircled O_{cus} vacancies in the lattice undergo a characteristic contrast reversal for bias voltages inside the conduction band (bright) and the oxide band gap (dark).

4 Theoretical Results

To construct an atomistic model consistent with these experimental observations, we have considered a large set of surface configurations compatible with the $(\sqrt{3} \times \sqrt{3})R30°$ unit cell by introducing both ad- and missing species in surface and sub-surface trilayers of the stoichiometric and Cu-deficient terminations. The surface energies of the key low energy configurations discussed in the following are plotted as a function of oxygen chemical potential in Fig. 5, while a complete set is shown in the SI (Fig. S2).

Before entering into the details of the phase diagram, let us note the substantially different sequences of relative stability predicted by HSE and GGA. Not only is the predicted most stable configuration not the same, but also the relative stability of the simple stoichiometric and Cu-deficient terminations as well as the position of the bulk Cu_2O stability limit visibly differ. As pointed out in Ref.[13] hybrid calculations tend to better reproduce the experimental value of the bulk Cu_2O stability limit and, due to a better account of the $Cu_2O(111)$ band gap and surface ionization potential, they avoid the serious underestimation of surface energy of the Cu-deficient termination which is otherwise over-stabilized by GGA.

Figure 5 proves that both the ST-O_s or CuD-O_s vacancy models proposed in the literature are thermodynamically unstable in both GGA and HSE approaches, due to the large cost of oxygen vacancy formation at the $Cu_2O(111)$ surface. Indeed, filling the surface vacancy with an oxygen atom transforms them into the (1×1) stoichiometric (ST) or Cu-deficient (CuD) terminations, respectively, and brings a very substantial gain in stability. Interestingly, the energy cost to create surface oxygen vacancies is systematically about 0.9 eV/vacancy larger in the HSE approximation than in GGA, in line with larger HSE oxygen vacancy formation energy in bulk Cu_2O. Moreover, the comparison between X-O_s and X-O_{ss} energies in Figure 5 (with X=ST or CuD) shows that moving the oxygen vacancy from the surface to the subsurface site directly below the surface Cu_{cus} cation

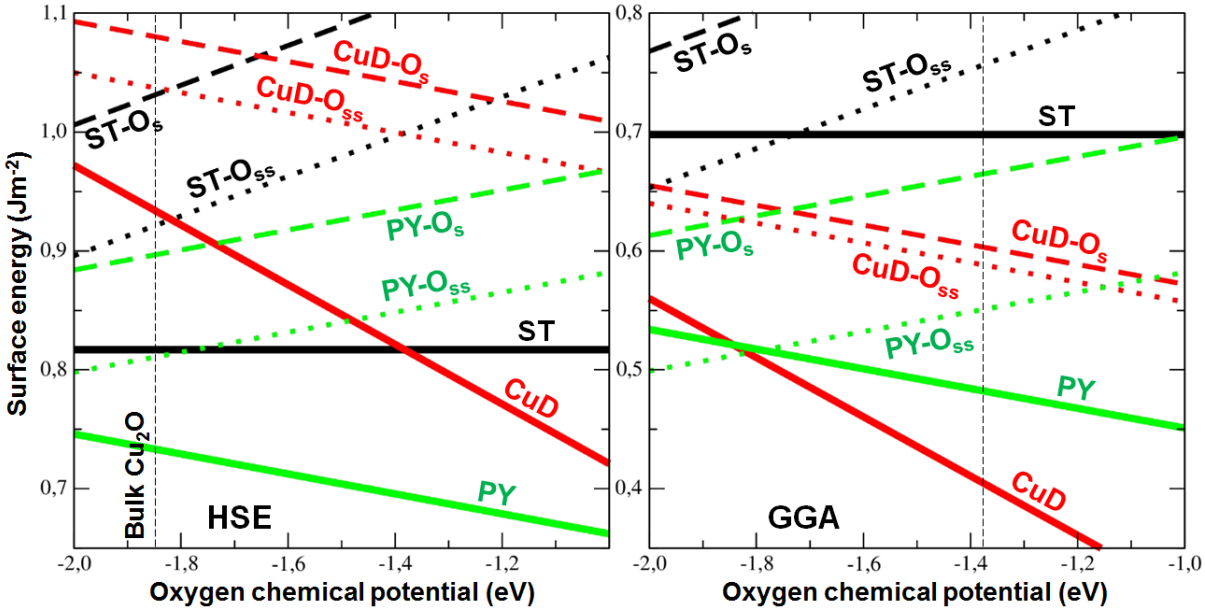

Figure 5: Calculated HSE (left) and GGA(right) surface energies of various $(\sqrt{3} \times \sqrt{3})$R30° model reconstructions of the $Cu_2O(111)$ surface, plotted as a function of oxygen chemical potential. The labels "-O_s" and "-O_{ss}" refer to configurations with surface and subsurface oxygen vacancies, respectively (see text).

is energetically favored by 0.3/0.1 eV/vacancy (HSE/GGA), although this energy gain is insufficient to allow the resulting configuration to compete with the most stable ones in the phase diagram.

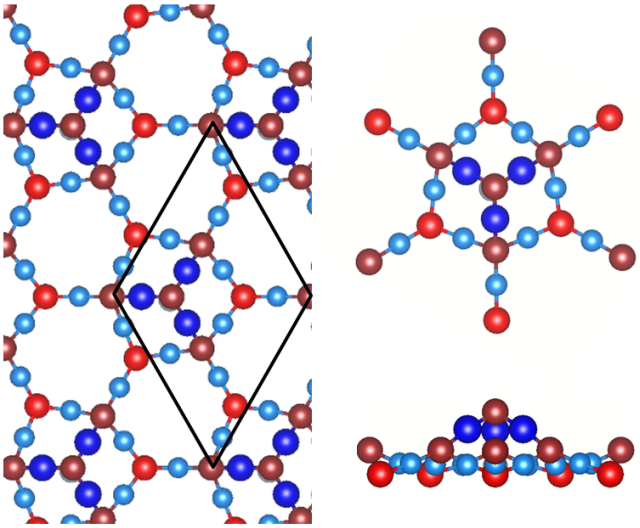

Figure 6: Atomistic representation of the pyramidal reconstruction (PY) of the $(\sqrt{3} \times \sqrt{3})$R30° $Cu_2O(111)$ surface. Left: top view of the $(\sqrt{3} \times \sqrt{3})$R30° unit cell. Right: Top and side views of a nanopyramid at the center of a Cu_6O_6 ring. Same color code as in Fig. 1

.

In contrast, a surface configuration obtained by adding Cu_4O entities at the center of one-third of the surface rings at the Cu-deficient termination (configuration denoted PY in Figure 5) is by far the most stable one in HSE in a wide range of oxygen conditions. Its atomistic representation is shown in Fig. 6. It features Cu_4O nano-pyramids formed by three copper adatoms located at the center of the Cu_6O_6 rings, capped by an oxygen atom and with a Cu_{cus} atom below. The three outermost Cu adatoms (distant by 2.8 Å from each other) protrude above the surface O_{cus} atomic plane by about 1 Å and point toward the surface O_{cus} atoms. The capping oxygen atom is located 1 Å above these three Cu. This pyramidal model of the $(\sqrt{3} \times \sqrt{3})$R30° reconstruction thus agrees with the experimental location, the topographic height, and the orientation of shamrock features.

According to the HSE results, the stability enhancement of the PY configuration with respect to the Cu-deficient termination originates from the reduced number of under-coordinated O_{cus} atoms (from three to one per unit cell) and from the reduced formal surface charge excess at these polar terminations.[25] While we are not

aware of an existing theoretical prediction of such configuration on the $Cu_2O(111)$ surface, it bears a topological similarity to the (3,3;1,0) reconstruction proposed for the (100) orientation,[5] and with the Cu_3O entities seen during the growth of Cu_2O on Pt(111).[26]

5 Discussion

5.1 Comparison Between Experimental and Simulated STM Images

In order to substantiate the relevance of the nanopyramid model as the likely structure of the $(\sqrt{3} \times \sqrt{3})R30°$ reconstruction besides stability considerations, we now confront simulated STM images of the pyramidal (PY) and the two vacancy (CuD-O_s and ST-O_s) models, Figure 7, with experimental STM images (Figures 2 and 3).

As expected, the shamrock pattern produced by the PY model is correctly centered in the middle of the surface hexagonal rings and, as in the experimental images, its lobes point toward the neighboring O_{cus} atoms. The three Cu adatoms which protrude above the surface O_{cus} atomic plane produce three distinct lobes at negative bias, with a bright spot superimposed at their center, which corresponds to the capping oxygen atom. At positive bias, the shamrock pattern is less distinct. The simulated STM contrast is dominated by the capping oxygen atoms and approaches closely the single-spot image observed experimentally for some tip shapes and/or bias values (Fig. 3c). Thus, the PY model of the $(\sqrt{3} \times \sqrt{3})R30°$ reconstruction not only agrees with the experimental observation by its position and orientation on the surface but also by a weakly bias dependent STM contrast principally driven by topographic effects.

Conversely, the vacancy models produce a STM contrast centered at one corner of the surface rings and strongly dependent on bias. This is very clear in the ST-O_s configuration, where, similarly to the stoichiometric surface, the positive bias contrast is dominated by the contri-

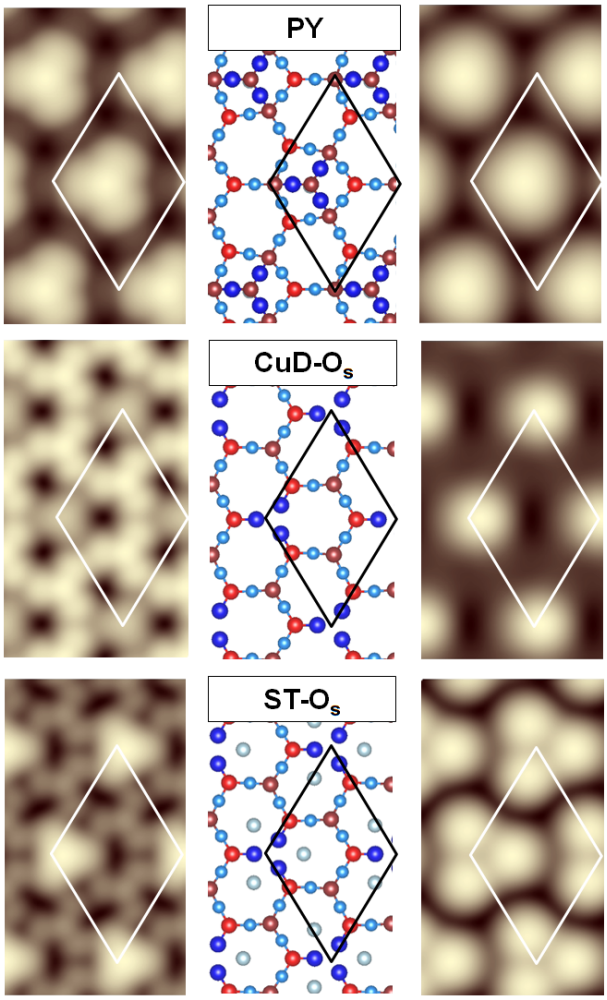

Figure 7: From top to bottom, simulated constant current STM images of the pyramidal PY, vacancy CuD-O_s and vacancy ST-O_s models of the $Cu_2O(111)$ $(\sqrt{3} \times \sqrt{3})R30°$ reconstruction, at negative and positive biases (left and right of the atomistic representations, respectively).

bution of empty s state of Cu_{cus} (see SI, Figure S3). The resulting spot distance of 4.7 Å is close to the geometrical distance between the Cu_{cus} ions (4.9 Å). Conversely, negative bias contrast is rather due to the filled d_{z2} states at the same Cu_{cus} atoms, which dramatically reduces the separation of the three maxima.

Electronic effects are even more striking in the STM image of the CuD-O_s configuration, where the overall weak contrast resembles closely that of the pristine Cu-deficient surface. Due to the proximity of Cu_{csa} atoms around the vacancy (2.5 Å), their empty s states (Figure S3) do not produce the three clearly separated spots, characteristic of the observed shamrock reconstruction (Fig. 3c). The O_{cus} vacancy thus rather appears as a single spot in the simulated STM image. At negative bias, the nearly in-plane orientation of the Cu-O bonds makes the occupied Cu d_{z2} orbitals of the three terminal Cu atoms point towards the vacancy rather than out of the surface plane, making the three atoms hardly visible. The contrast reversal between positive and negative polarity agrees with experimental STM images of the few observed oxygen vacancies (Figure 4).

In summary, the STM signatures of the CuD-O_s and ST-O_s vacancy models of the $(\sqrt{3} \times \sqrt{3})$R30° reconstruction are in sound disagreement with the experimental results, regarding the shamrock location, topographic height and orientation with respect to the surface rings, as well as their strongly bias-dependent STM contrast of mainly electronic origin. Conversely, the STM signature of the proposed pyramidal model PY matches very satisfactorily the experiment. Not only is the shamrock structure correctly located and oriented with respect to the $Cu_2O(111)$ lattice but also its STM contrast is principally driven by topographic effects thus producing a relatively weak bias dependence.

5.2 Oxygen Vacancies at the $Cu_2O(111)$ Surface

Figure 5 reveals an unexpected peculiarity of surface oxygen vacancies. Indeed, whether starting from the pyramidal, the stoichiometric or the Cu-deficient structures, all configurations with surface oxygen vacancies are unstable with respect to moving the vacancy sub-surface. For example, while the formation of an oxygen vacancy on the top of the Cu_4O entity in the PY configuration requires a high energy, much less energy (reduction of 0.6/0.7 eV/vacancy in HSE/GGA) is needed if the vacancy is instead created in the subsurface site just below the Cu_{cus} cation.

Such strong preference for sub-surface vacancy location at the $Cu_2O(111)$ surface is shared by no other sub-surface or bulk site. It is quite unusual and, to our knowledge, it has not been previously recognized. Indeed, in a large variety of materials of very different nature, vacancy formation energies grow with the number of broken bonds, which gives a strong bias for vacancies to segregate at surfaces. In the present case, although four O-Cu bonds are broken in the sub-surface site compared to three at the $Cu_2O(111)$ surface, our results reveal the existence of an electronic mechanism, quasi-independent of the HSE/GGA approximation, which opposes and overrides the usual coordination effect. It is related to the different localization of the two electrons left by the removed oxygen at the surface and sub-surface sites. In the former case, they are evenly distributed over the 3 nearest-neighbor Cu cations, resulting in their partial metallization and fractional oxidation state. In contrast, in the case of a sub-surface vacancy below a Cu_{cus} atom, this Cu_{cus} cation participates to the electron accommodation, to the point of becoming practically neutral, and the charge modification of the three other neighbors is much smaller. As a consequence, despite its charge neutrality and the absence of O-Cu bonds, this Cu_{cus} atom remains strongly trapped in the center of the surface ring. Indeed, when surface Cu_{cus} cations are absent, for example in the CuD-O_s configuration, the energy gain of moving the O vacancy to sub-surface is significantly reduced (Figure 5), which clearly highlights the peculiar role of surface Cu_{cus} ions in the unusual behavior of vacancies at the $Cu_2O(111)$ surface. Such electronic stabilization presents some similarity with the electron localization around subsurface oxygen vacancies found in defective ce-

ria films.[27]

6 Conclusion

By a combination of high-resolution STM measurements and numerical simulations based on a DFT-HSE approach, we challenge the previous interpretations of the $Cu_2O(111)$ $(\sqrt{3} \times \sqrt{3})R30°$ surface reconstruction. We show that the existing models do not meet the STM observations, that is shamrock features located at the Cu-O ring centers, orientation of the spots towards the surface O_{cus} atoms and topographic nature of the STM contrast. Moreover, they are thermodynamically unstable, due to the preference, not recognized before, of oxygen vacancies to locate sub-surface rather than in the surface plane. We propose a new model of the $(\sqrt{3} \times \sqrt{3})R30°$ surface reconstruction in which the shamrock protrusions seen in STM are formed by nanopyramids made of three copper adatoms located at the center of the Cu-O rings above the Cu_{cus} atoms and capped by an oxygen atom.

In a broader perspective, we find that the relative stability pattern of the various surface terminations may be rationalized by two main effects: (i) a strong thermodynamic bias for oxygen vacancy filling which might be one cause for the p-type conductance of Cu_2O and (ii) a clear preference for sub-surface rather than surface oxygen vacancies. While the first effect is much more pronounced in HSE, in line with larger HSE bulk oxygen vacancy formation energy, the second one relies on the enhanced capacity of the surface Cu_{cus} atoms to accommodate an electron excess and is independent of the level of approximation. These effects are responsible for the thermodynamic instability of the vacancy models and result in an enhanced stability of the pyramidal $(\sqrt{3} \times \sqrt{3})R30°$ reconstruction, being even more stable than the known (1×1) configurations.

A $Cu_2O(111)$ surface model that is not based on low-coordinated Cu_{cus} ions anymore will drastically change common interpretation schemes of the surface reactivity of cuprous oxide.

7 Acknowledgments

Financial support from the DFG grant Ni 650-5 *Towards an atomic-scale understanding of ideal, defective and doped cuprous oxide surfaces and interfaces* is gratefully acknowledged.

8 Supporting Information

The Supporting Information is available free of charge at XXX.

It gives additional information on theoretical results, concerning the stability of several Cu_2O (111) (1×1) and $(\sqrt{3} \times \sqrt{3})R30°$ configurations, their simulated STM images and their Local Densities of States (LDOS) (pdf).

References

(1) Schulz, K. H.; Cox, D. F. Photoemission and low-energy-electron-diffraction study of clean and oxygen-dosed Cu_2O (111) and (100) surfaces. *Physical Review B* **1991**, *43*, 1610.

(2) Nygren, M. A.; Pettersson, L. G.; Freitag, A.; Staemmler, V.; Gay, D. H.; Rohl, A. L. Theoretical models of the polar Cu_2O (100) Cu^+-terminated surface. *The Journal of Physical Chemistry* **1996**, *100*, 294–298.

(3) McClenaghan, N. D.; Hu, P.; Hardacre, C. A density functional theory study of the surface relaxation and reactivity of Cu_2O (100). *Surface science* **2000**, *464*, 223–232.

(4) Le, D.; Stolbov, S.; Rahman, T. S. Reactivity of the Cu_2O (100) surface: Insights from first principles calculations. *Surface science* **2009**, *603*, 1637–1645.

(5) Soldemo, M.; Stenlid, J. H.; Besharat, Z.; Ghadami Yazdi, M.; Önsten, A.; Leygraf, C.; Gothelid, M.; Brinck, T.; Weissenrieder, J. The surface structure of Cu_2O (100). *The Journal of Physical Chemistry C* **2016**, *120*, 4373–4381.

(6) Zhang, R.; Li, L.; Frazer, L.; Chang, K. B.; Poeppelmeier, K. R.; Chan, M. K.; Guest, J. R. Atomistic determination of the surface structure of Cu_2O (111): experiment and theory. *Physical Chemistry Chemical Physics* **2018**, *20*, 27456–27463.

(7) Jensen, F.; Besenbacher, F.; Stensgaard, I. Two new oxygen induced reconstructions on Cu (111). *Surface science* **1992**, *269*, 400–404.

(8) Sträter, H.; Fedderwitz, H.; Gross, B.; Nilius, N. Growth and surface properties of cuprous oxide films on Au (111). *The Journal of Physical Chemistry C* **2015**, *119*, 5975–5981.

(9) Ly, T. T.; Lee, T.; Kim, S.; Lee, Y.-J.; Duvjir, G.; Jang, K.; Palotás, K.; Jeong, S.-Y.; Soon, A.; Kim, J. Growing ultrathin Cu_2O films on highly crystalline Cu (111): a closer inspection from microscopy and theory. *The Journal of Physical Chemistry C* **2019**, *123*, 12716–12721.

(10) Soon, A.; Todorova, M.; Delley, B.; Stampfl, C. Surface oxides of the oxygen–copper system: Precursors to the bulk oxide phase? *Surface Science* **2007**, *601*, 5809–5813.

(11) Islam, M. M.; Diawara, B.; Maurice, V.; Marcus, P. First principles investigation on the stabilization mechanisms of the polar copper terminated Cu_2O (111) surface. *Surface Science* **2009**, *603*, 2087–2095.

(12) Li, C.; Wang, F.; Li, S.; Sun, Q.; Jia, Y. Stability and electronic properties of the O-terminated Cu_2O (111) surfaces: First-principles investigation. *Physics Letters A* **2010**, *374*, 2994–2998.

(13) Nilius, N.; Fedderwitz, H.; Groß, B.; Noguera, C.; Goniakowski, J. Incorrect DFT-GGA predictions of the stability of non-stoichiometric/polar dielectric surfaces: The case of Cu_2O (111). *Physical Chemistry Chemical Physics* **2016**, *18*, 6729–6733.

(14) Önsten, A.; Göthelid, M.; Karlsson, U. O. Atomic structure of Cu_2O (111). *Surface Science* **2009**, *603*, 257–264.

(15) Bendavid, L. I.; Carter, E. A. First-principles predictions of the structure, stability, and photocatalytic potential of Cu_2O surfaces. *The Journal of Physical Chemistry B* **2013**, *117*, 15750–15760.

(16) Kresse, G.; Hafner, J. Ab initio molecular dynamics for liquid metals. *Phys. Rev. B* **1993**, *47*, 558–561.

(17) Kresse, G.; Furthmuller, J. Efficient iterative schemes for ab initio total energy calculations using a plane-wave basis set. *Phys. Rev. B* **1996**, *54*, 11169–11186.

(18) Perdew, J. P.; Burke, K.; Ernzerhof, M. Generalized gradient approximation made simple. *Physical review letters* **1996**, *77*, 3865.

(19) Heyd, J.; Scuseria, G.; Ernzerhof, M. Hybrid functionals based on a screened Coulomb potential. *J. Chem. Phys* **2003**, *118*, 8207–8215.

(20) Heyd, J.; Scuseria, G.; Ernzerhof, M. Erratum: "Hybrid functionals based on a screened Coulomb potential" [J. Chem. Phys. 118, 8207 (2003)]. *J. Chem. Phys* **2006**, *124*, 219906–219906.

(21) Meyer, B.; Polity, A.; Reppin, D.; Becker, M.; Hering, P.; Klar, P.; Sander, T.; Reindl, C.; Benz, J.; Eickhoff, M. et al. Binary copper oxide semiconductors: From materials towards devices. *physica status solidi (b)* **2012**, *249*, 1487–1509.

(22) Kresse, G.; Joubert, D. From ultrasoft pseudopotentials to the projector augmented-wave method. *Phys. Rev. B* **1999**, *59*, 1758–1775.

(23) Reuter, K.; Scheffler, M. Composition, structure, and stability of RuO_2 (110) as a function of oxygen pressure. *Physical Review B* **2001**, *65*, 035406.

(24) Monkhorst, H.; Pack, J. Special points for Brillouin-zone integrations. *Phys. Rev. B* **1976**, *13*, 5188–5192.

(25) Goniakowski, J.; Finocchi, F.; Noguera, C. Polarity of oxide surfaces and nanostructures. *Reports on Progress in Physics* **2007**, *71*, 016501.

(26) Gloystein, A.; Nilius, N. Copper Oxidation on Pt (111)—More than a Surface Oxide? *The Journal of Physical Chemistry C* **2019**, *123*, 26939–26946.

(27) Jerratsch, J.-F.; Shao, X.; Nilius, N.; Freund, H.-J.; Popa, C.; Ganduglia-Pirovano, M. V.; Burow, A. M.; Sauer, J. Electron localization in defective ceria films: A study with scanning-tunneling microscopy and density-functional theory. *Physical review letters* **2011**, *106*, 246801.

Graphical TOC Entry